Electronic Supplementary Material (ESI) for ChemComm.

Supplemental Information: Synthesis and chemical stability of technetium nitrides

Emily Siska,[†] Dean Smith,[‡] Ashkan Salamat,[*,†] Keith V. Lawler,[†]

Barbara Lavina,[‡] Frederic Poineau,[†] and Paul M. Forster[†]

†*Department of Chemistry & Biochemistry, University of Nevada Las Vegas, Las Vegas, Nevada 89154, USA*

‡*Department of Physics & Astronomy, University of Nevada Las Vegas, Las Vegas, Nevada 89154, USA*

¶*HPCAT, X-ray Science Division, Argonne National Laboratory, Illinois 60439, USA*

E-mail: salamat@physics.unlv.edu

Methods

Caution! Technetium-99 is a weak β-emitter (E_{max} = 292 keV). All manipulations were performed in a laboratory designed for handling radioactive materials using efficient HEPA-filtered fume hoods, glovebox techniques, and following locally-approved radiochemistry handling and monitoring procedures. Technetium metal, prepared from the thermal treatment of TcO_2 under hydrogen atmosphere was used for the experiment.[1]

^{99}Tc metal was prepared in a radiochemistry laboratory at UNLV as described elsewhere.[2] Tc metal, which can be described as polycrystalline aggregates, were loaded into DACs using rhenium or steel gaskets and diamonds with culets ranging from 250 μm - 600 μm. Nitrogen was either gas loaded using our in-house gas loading system or cryogenically. Ruby and/or gold were used as pressure markers. Figure S1 shows a typical sample loading in a DAC.

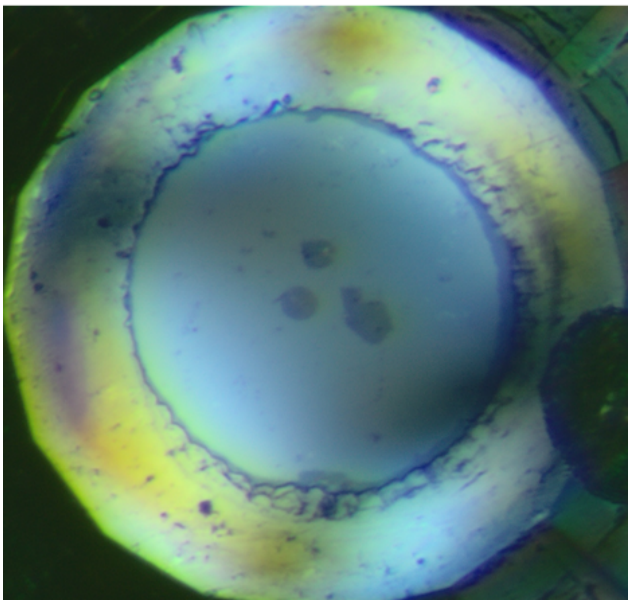

Figure S1: Image of a typical sample loading. Tc aggregates are placed on the center of a culet inside a gasket, which comprises the sample chamber. Gas is loaded, as a critical fluid, to fill the chamber.

Upon reaching a target pressure, samples were heated using the online laser (Nd:YAG) heating system at 16-ID-B (HPACT, APS) and 13-ID-D (GSE-CARS, APS) experimental stations. Progression of synthesis was observed by *in situ* x-ray diffraction (XRD) with a

0.4066 Å microfocused beam at HPCAT and a 0.3445 Å microfocused beam at GSE-CARS. Diffraction images were collected with either a Pilatus and a MAR detector. Data was reduced using Dioptas.[3] Full Rietveld refinements were performed using GSAS II.[4] Figure S2 shows representative XRD patterns of each Tc nitride.

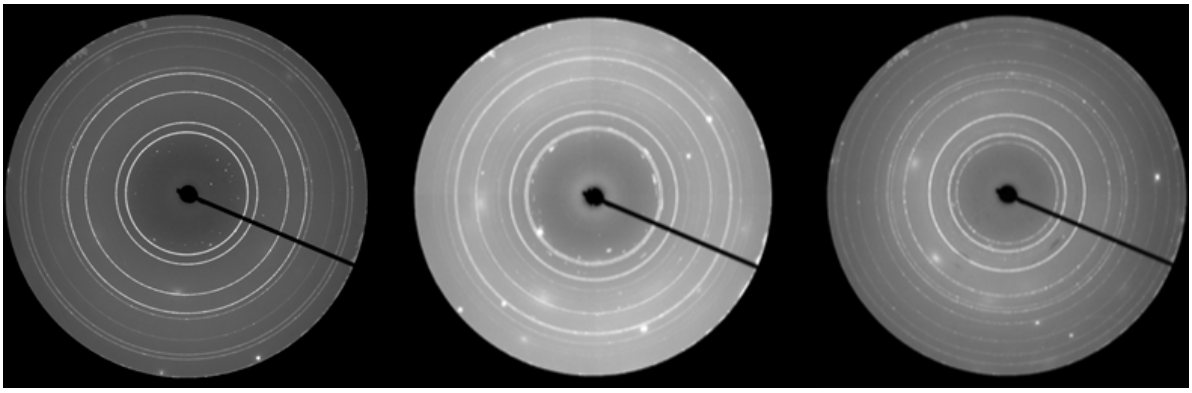

Figure S2: Two-dimensional image of diffraction patterns at 16.7 GPa, recorded at HPCAT (APS Sector 16, ANL) on a MAR345 area detector. Left: TcN_x. Middle: TcN. Right: Tc_2N.

Due to safety protocols at the APS, radioactive samples could not be decompressed or manipulated on site. Thus, the synthesized Tc_2N and TcN samples were decompressed and reloaded into another DAC at UNLV which was gas loaded with He and sent back to APS for subsequent equation of state analysis. Enough TcN_x sample was created to also prepare a DAC with no PTM for XRD anaylsis at ambient pressure, providing the pattern seen in Figure 2a of the main text. So although samples were brought to ambient conditions, XRD was not possible for Tc_2N and TcN at ambient pressure between transfer and gas loading. However, we are confident that both these samples are also recoverable to ambient conditions because all three high density phases are seen again at 2.2 GPa, after the recovery to ambient conditions. The likelihood of back transforming into a lower density phase at ambient and then back to their high density phases, all at the same pressures, without laser heating seems unlikely.

Equations of State

Tc_2N and TcN were recovered, reloaded in a helium medium, and compressed at room temperature to above 30 GPa in order to determine experimental equations of state. TcN_x was compressed at room temperature, directly after synthesis, in a nitrogen medium. The experimental P–V data was fit with a second order Birch-Murnaghan EOS as seen in Figure S3 with corresponding residuals. The refined V_0 and B_0 are in Table S1 ($B_0^{'}$ is fixed to 4). Third-order Birch-Murnaghan EOS fits were attempted, but the values for $B_0^{'}$ were over-fit to non-physical values due to the scatter in the data.

Table S1: Values from EOS fit to experimental data for all three compounds

		2^{nd} Order BM	
Compound	Space group	V_0 (Å^3/Tc atom)	B_0 (GPa)
Tc	$P6_3/mmc$	14.305 (4)	321 (5)
TcN_x	$Fm\bar{3}m$	15.427 (2)	298 (4)
Tc_2N	$P6_3/mmc$	16.758 (9)	342 (8)
TcN	$Pnma$	19.345(9)	322 (6)

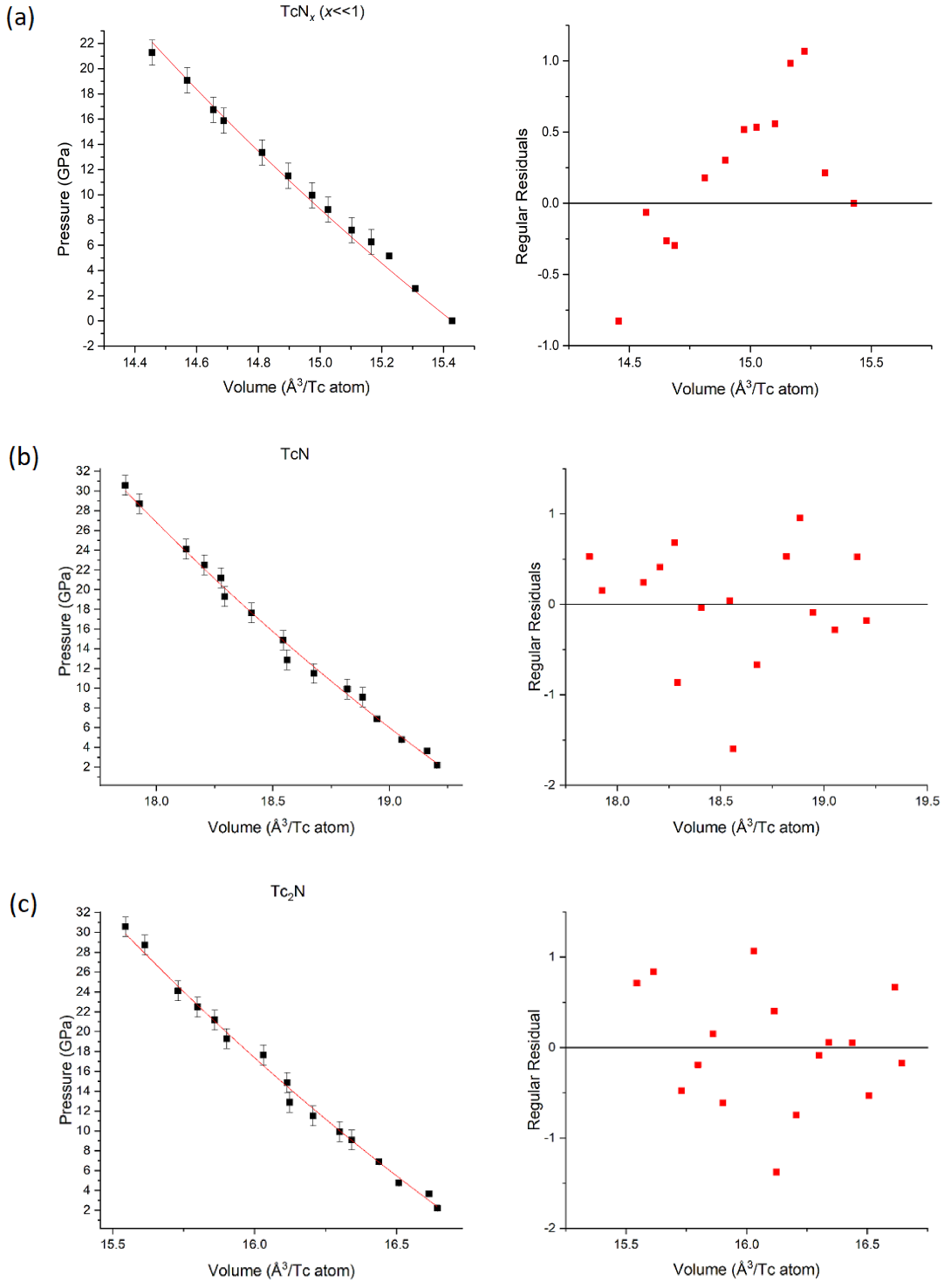

Figure S3: **Left** Compression data shown with Birch-Murgahan EOS fit and pressure error bars. **Right** Corresponding of residuals for EOS fit shown for each nitride.

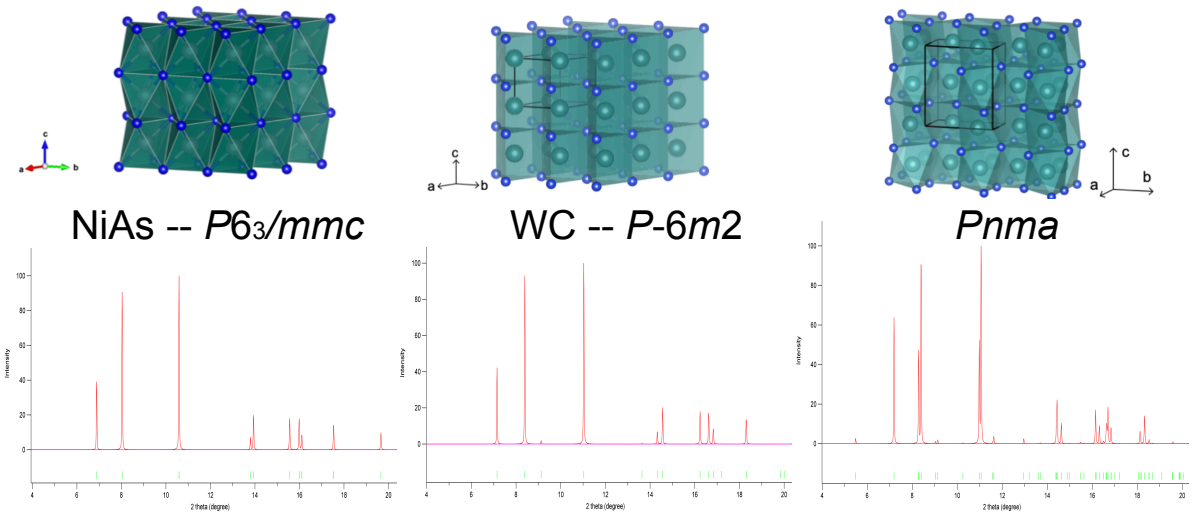

Figure S4: Structural representations and corresponding simulated diffraction patterns from our DFT calculations of three proposed structure solutions for TcN. All are at 40 GPa, with $\lambda = 0.3445$ Å

Simulations

Plane-wave density functional theory (PW-DFT)[5,6] simulations were performed with the Vienna *ab initio* simulation package (VASP) version 5.4.4 using the generalized gradient approximation (GGA) functional of Perdew, Burke and Ernzerhof (PBE).[7] Simulations were performed with and without a single-parameter Hubbard "+U" correction[8–10] applied to the Tc d electrons to determine if an overly weak description of electron correlation affected the energy orderings and predicted structures. The U_{eff} used here was 3.5 eV, halfway between the U_{eff}=2.95 eV determined by a linear response approach[11] for the ambient hcp phase of Tc and the $\geq$ 4 eV[12] shown to be necessary to predict the band gaps of Tc oxide materials. The simulations used an evenly space Γ–centered k-point grid with 0.2 $Å^{-1}$ resolution.[13] As the system is metallic, the Brillouin zone was integrated the first order method of Methfessel and Paxton with a width of 0.10 eV.[14] The basis set cutoff energy was 550 eV using the projector augmented wave (PAW)[15] pseudo-potentials formulated for PBE (version 5.4) with valence configurations of $4p^6 5s^2 4d^5$ for Tc (ie. "Tc_pv"), $2s^2 2p^3$ for N. Energy convergence tolerances for the self-consistent field steps were set to 10^{-9} eV and force convergence tolerances for the geometry optimizations to 10^{-3} eV $Å^{-1}$. To minimize the effect of Pulay stress, the volume changing structural optimizations were performed in three parts: two sequential optimizations and a final single point energy evaluation. Band structure plots were created with the sumo package[16] by re-determining the bands along a cell's respective high symmetry points and lines[17] using a fixed charge density that was pre-converged over an evenly spaced k-point mesh. The phonon dispersion was evaluated with density functional perturbation theory using a 4×4×3 supercell of the NiAs structure and a 4×3×2 supercell of the *Pnma* structure (both 192 atom cells).[18] The phonon plots were constructed using the phonopy[19] package.

A previous first attempt to estimate the stoichiometry of TcN_x was done with non-spin-polarized DFT optimizations of integer numbers of *fcc* Tc unit cells with a single nitrogen atom inserted on an octahedral interstitial site.[20] A non-magnetic cell of Tc_4N (3.5 wt%

N) maintains a cubic structure with a volume beyond (16.10 Å^3/Tc) what was measured for either β-Tc or TcN_x, but by 0.5 wt% N (3 at%, 1 N in a 2×2×2 supercell) the unit cell volume is too small (14.62 Å^3/Tc) compared to what is measured. The non-magnetic simulations suggest a stoichiometry close to Tc_8N based on agreement of the optimized volume (15.2 Å^3 per Tc) versus the EOS determined V_0 for TcN_x (15.4 Å^3 per Tc). However, this model neglects any electron correlation effects that could be driving the anomalous properties of β-Tc and should be viewed as an upper estimate of the nitrogen content of TcN_x. This is exemplified by Tc_8N having a nitrogen content of 11 atom %, yet the EDX measurements dictate a nitrogen content of 0–2%.

Our current hypothesis is that β-Tc is best regarded as a high temperature phase of Tc which is *fcc* in its high temperature paramagnetic phase and antiferromagnetically (AFM) orders and tetragonally distorts into a *bct* structure as it crosses its Néel temperature somewhere above 300 K.[20,21] Such a distortion implies AFM type-I ordering similar to γ-Mn (with spins anti-parallel along the [001] easy axis) as is confirmed to be the most favorable ordering by DFT+U calculations.[22–25] Building on this hypothesis, TcN_x might retain some of the potential magnetic properties of β-Tc. Optimizing an AFM supercell with N impurities in the form of insertion onto an octahedral interstitial site in general leads to a ferrimagnet with slightly diminished average atomic moments, where larger doping concentrations appear cubic but smaller concentrations tetragonally distort. A coarse scan of uniform supercells shows that a slight volume reduction (0.2%) compared to the undoped AFM lattice is observed with a 3×3×3 *fcc* supercell with a single N atom on an octahedral interstitial site (0.9 at%), although the lattice still tetragonally distorted. In this model the computed per Tc magnetic moment reduced to 1.813 μ_B from the 1.909 μ_B of the undoped cell. Another potential model for TcN_x is that nitrogen defects to β-Tc come in the form of a N substitution of a Tc atom. Our preliminary calculation of a single substitution defect in an 2×2×2 *fcc* supercell produced a tetragonally distorted ferrimagent (1.870 μ_B average moment) with a volume only 1.6% larger than that of the parent lattice. Antiferromagneti-

cally ordered Cr exhibits a volume contraction as it is heated through the first-order AFM to paramagnetic (PM) transition, and doping Cr with 5 wt% V suppresses that transition keeping the system in the high temperature lower volume phase.[26] Thus, doping AFM β-Tc with N either interstitially or as a substitution could similarly be suppressing the magnetic ordering transition and maintaining a smaller per Tc volume, since the β-Tc and TcN_x lattices are fcc and very likely paramagnetic at the high temperatures where they are formed. Further simulations are underway to understand the thermal effects on the volumetric and magnetic properties of β-Tc and TcN_x (including differing supercell sizes and site placement of the defects), however these preliminary results indicate that low quantity N doping would not quench the electron correlation driving the magnetism but could disrupt its ordering.

While it is rare for materials to exhibit a volume contraction when doped, it is not entirely unheard of. For instance, both fcc and bcc phases of iron have been observed decrease their molar volumes when carbon is doped into the lattice, for fcc the carbon is believed to occupy octahedral interstitial sites like in our initial model for TcN_x.[27,28] Recently, it was shown that the introduction of low doses of hydrogen into gold also leads to a volume contraction explained by the initial formation of hydride bonds.[29] Another example relevant to our hypothesis of magnetism in β-Tc is $Sm_2Mn_8Al_9B_x$, which exhibits a non-monotonic altered magnetic moment and contracted volume for $0<x<1$.[30] These examples highlight that interactions such as bonding or perturbed magnetism can lead to volume contractions, and there is on-going work to determine the nature of these interactions TcN_x.

Crystal structure prediction (CSP) using the USPEX v10.2[31–33] package was necessary as the degree of crystallinity for the TcN phase was not sufficient to do *ab initio* indexing. Additionally, the structural models predicted by Kim et al. and others do not correctly describe the experimental X-ray diffraction data observed for this phase.[34–36] The most clear indication of a mismatch from other predictions is the lowest 2θ feature at 6 degrees is not accounted for in either the predicted NiAs, $R\bar{3}m$, or WC structures shown to be favorable candidates in the previous theoretical studies. The USPEX structure searches targeted only

the TcN stoichiometry with Z=1–4 and Z=6 formula units per unit cell. There were 20 structures per generation and all of the previously predicted structures[34–36] were seeded in the first generation of their respective search. The crystal structure predictions all employed the single parameter Hubbard "+U" correction, but all determined structures of interest were re-optimized with and without said correction. Table S2 provides the relative stability of the previously predicted and newly discovered possible phases of TcN. The "+U" correction was found to have little effect on the energy orderings of the structures, as can be seen in Table S3. A newly identified *Pnma* structure is predicted with a Tc_4N_4 (Z=4) unit cell. The *Pnma* structure is closely related to the NiAs structure which is in turn related to the WC structure as can be seen in Figure S4. All the Bragg features in the experimental XRD pattern and a full Rietveld analysis of TcN is made possible with this model.

The hexagonal unit cell of the NiAs structure can be transformed into an orthogonal representation to facilitate comparing it with the *Pnma* structure. The goal is to convert γ from 120° to 90°, so only the a and b axes need to be transformed, the c axis can remain the same. The left panel of Figure S5 shows a common way to draw the new orthogonal a' and b' axes from a supercell representation of the original hexagonal structure.[37] An alternate way to draw the orthogonal box is shown in the right panel of Figure S5, and it is the one used here to simplify aligning it with the TcN *Pnma* cell.[38] Either orthorhombic representation is an effective supercell of the hexagonal primitive cell which doubles the number atoms. In both cases, the length of a' is the same as a, and the length of b' is $\sqrt{3}$ times that of b. A final step to simplify the comparison of the orthorhombic NiAs structure (Figure S6 left) is to shift its origin to be commensurate with that of the *Pnma* TcN structure. The shift required is $\left(-\frac{1}{4}, -\frac{1}{4}, 0\right)$ with the final structure shown in the right panel of Figure S6 and fractional atomic coordinates reported in Table S5. Note that what is shown in Figure S6 and Table S5 is the non-standard *Pmcn* setting of space group 62 as set by our symmetrizing utility when applied to the CSP determined structure; the XRD determined lattice and positions in the main text are described in the standard *Pnma* setting of space group 62.

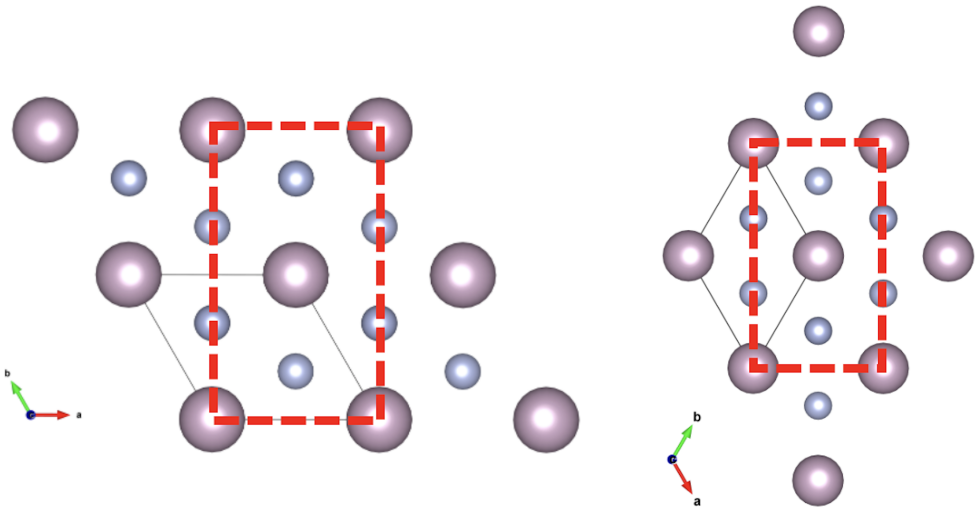

Figure S5: Two different approaches to define the a' and b' axes for an orthorhombic version of a hexagonal cell. Both approaches require a subset of a 2×2×1 supercell of the hexagonal cell. The key difference between them being the alignment of the b' axis, where one is the inverse of the other, ie. $b'_{\text{right}} = 1\text{-}b'_{\text{left}}$. The approach shown on the right is used here to simplify aligning it with the TcN *Pnma* cell.

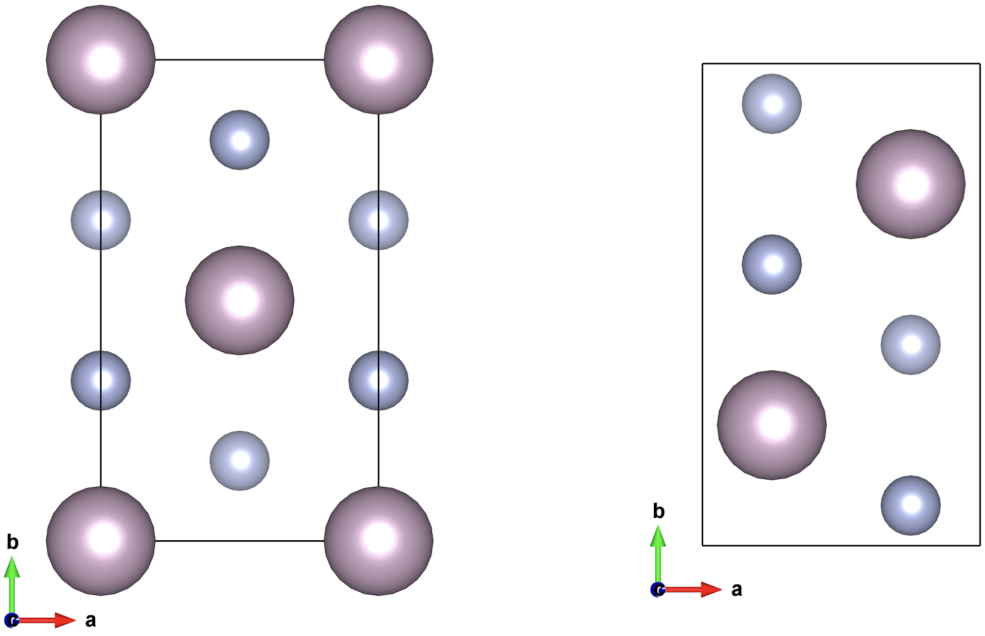

Figure S6: To facilitate direct visual comparison of the orthorhombic transformation of the NiAs TcN structure (left) with the *Pnma* structure, the origin of the transformed structure is shifted by $\left(-\frac{1}{4}, -\frac{1}{4}, 0\right)$ to produce the right structure.

Table S2: PBE+U_{eff}=3.5 eV Relative Enthalpies of 40 GPa TcN Structures

	Z	H (eV/unit cell)	H/Z (eV/f.u.)	ΔH/Z (meV/f.u.)
$Pnma$	4	-39.077262	-9.769315	0.000
NiAs	2	-19.517723	-9.758861	10.454
$R\bar{3}m$	6	-57.326194	-9.554366	214.950
$Imm2$	6	-56.233012	-9.372169	397.147
NbO	3	-27.907718	-9.302573	466.743
WC	1	-9.101743	-9.101743	667.573
Diamond	1	-8.793264	-8.793264	976.051
Zincblende	4	-35.170990	-8.792748	976.568
NaCl	4	-35.101146	-8.775287	994.029
CsCl	1	-8.484679	-8.484679	1284.637
Wurtzite	2	-16.846948	-8.423474	1345.841

Table S3: PBE Relative Enthalpies of 40 GPa TcN Structures

	Z	H (eV/unit cell)	H/Z (eV/f.u.)	ΔH/Z (meV/f.u.)
$Pnma$	4	-55.720308	-13.930077	0.000
NiAs	2	-27.850833	-13.925417	4.661
$R\bar{3}m$	6	-83.087015	-13.847836	82.241
$Imm2$	6	-82.018127	-13.669688	260.389
NbO	3	-40.885861	-13.628620	301.457
WC	1	-13.413909	-13.413909	516.169
Diamond	1	-12.973655	-12.973655	956.422
Zincblende	4	-51.902804	-12.975701	954.376
NaCl	4	-51.873629	-12.968407	961.670
CsCl	1	-12.712738	-12.712738	1217.339
Wurtzite	2	-25.301294	-12.650647	1279.430

Table S 4: The symmetrized atomic positions for the PBE+U_{eff}=3.5 eV NiAs $P6_3/mmc$ structure of TcN at 40 GPa with lattice a=2.72781, b=2.72781, c=5.49008, α=β=90.000°, and γ=120.000°.

atom	a	b	c
Tc1	0.00000	0.00000	0.500000
Tc2	0.00000	0.00000	0.00000
N1	0.66667	0.33333	0.25000
N2	0.33333	0.66667	0.75000

Table S 5: The symmetrized atomic positions for the PBE+U_{eff}=3.5 eV NiAs structure of TcN at 40 GPa converted into an orthorhombic lattice of a=2.72781, b=4.72471, c=5.49008, and α=β=γ=90.000°.

atom	a	b	c
Tc1	0.25000	0.25000	0.00000
Tc2	0.25000	0.25000	0.50000
Tc3	0.75000	0.75000	0.00000
Tc4	0.75000	0.75000	0.50000
N1	0.25000	0.58333	0.75000
N2	0.25000	0.91667	0.25000
N3	0.75000	0.41667	0.25000
N4	0.75000	0.08333	0.75000

Table S 6: The symmetrized atomic positions for the PBE+U_{eff}=3.5 eV *Pnma* structure (in the *Pmcn* setting) of TcN at 40 GPa with lattice a=2.71539, b=4.75540, c=5.49046, and α=β=γ=90.000°.

atom	a	b	c
Tc1	0.25000	0.26386	0.00146
Tc2	0.25000	0.23614	0.50146
Tc3	0.75000	0.73614	0.99854
Tc4	0.75000	0.76386	0.49854
N1	0.25000	0.58093	0.73313
N2	0.25000	0.91907	0.23313
N3	0.75000	0.41907	0.26687
N4	0.75000	0.08093	0.76687

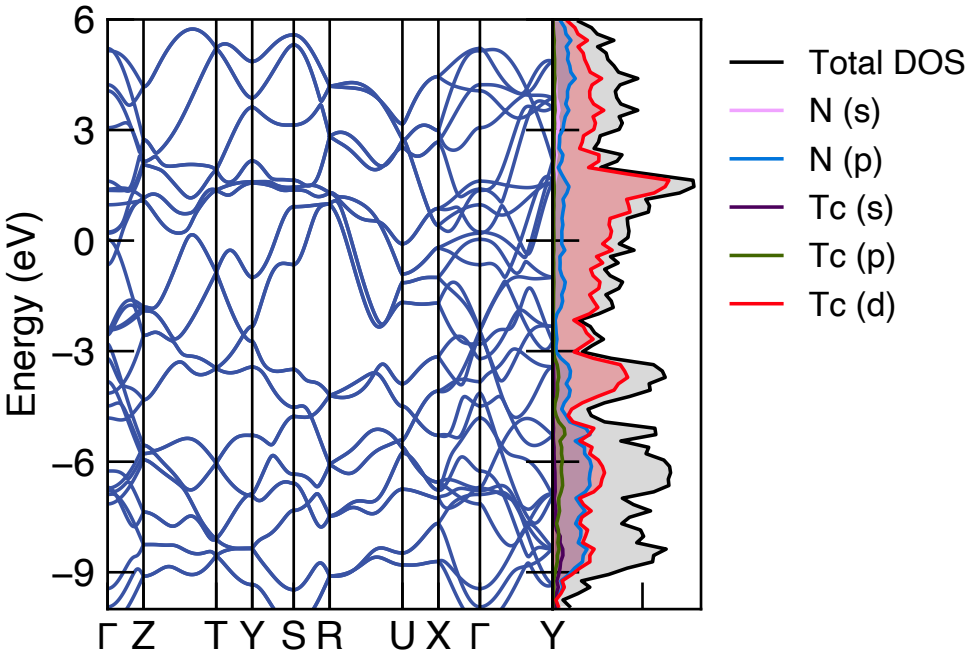

Figure S7: The PBE+U_{eff}=3.5 eV band structure and density of states for the *Pnma* structure of TcN at 40 GPa.

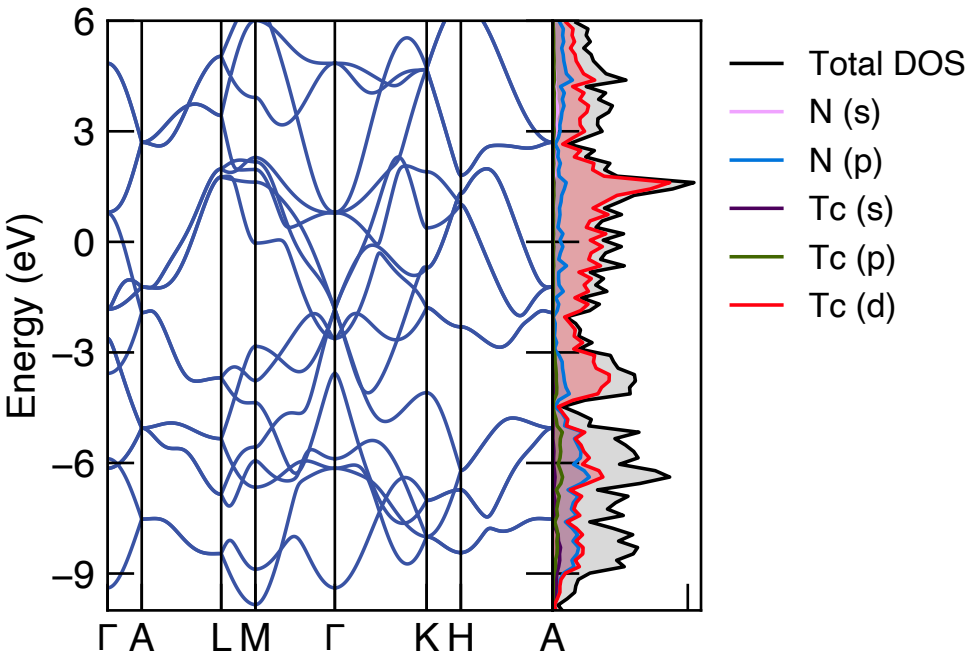

Figure S8: The PBE+U_{eff}=3.5 eV band structure and density of states for the NiAs structure of TcN at 40 GPa.

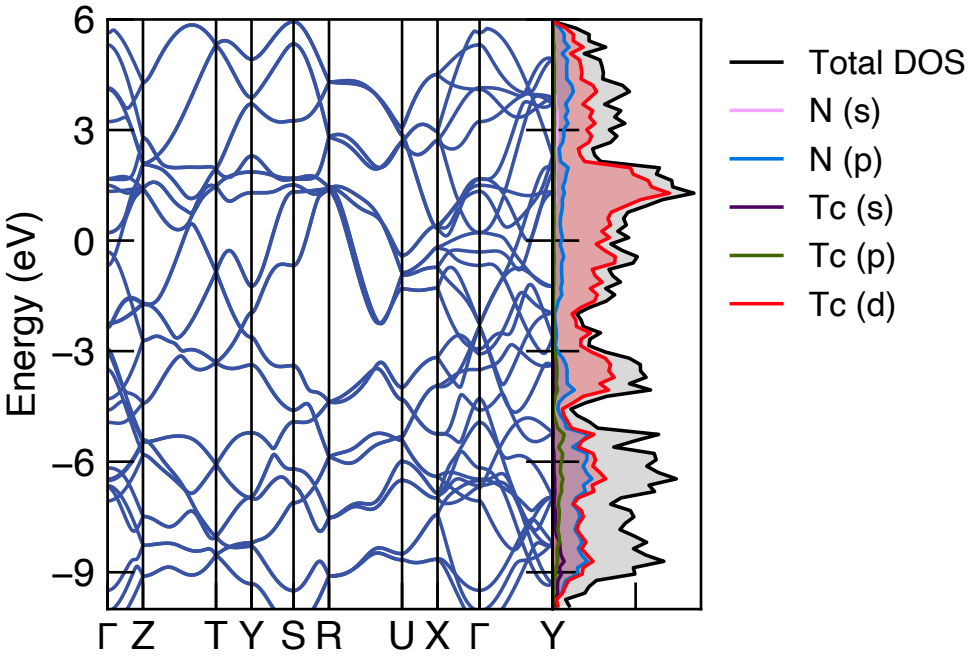

Figure S9: The PBE band structure and density of states for the *Pnma* structure of TcN at 40 GPa.

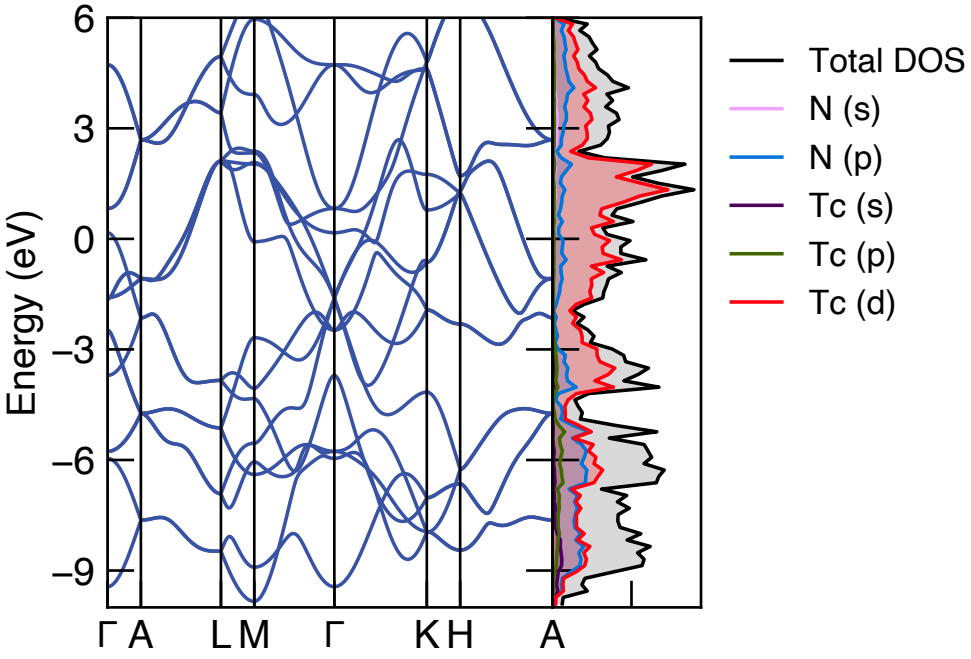

Figure S10: The PBE band structure and density of states for the NiAs structure of TcN at 40 GPa.

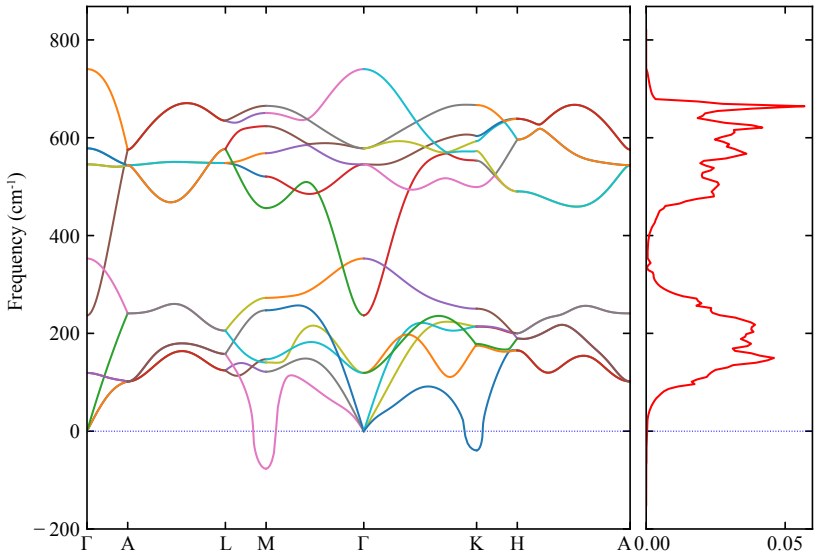

Figure S11: The PBE phonon band structure and density of states for the NiAs structure of TcN at 40 GPa. There are dynamic instabilities at the K and M high symmetry points and Kohn anomalies in the Γ–K and Γ–M directions.

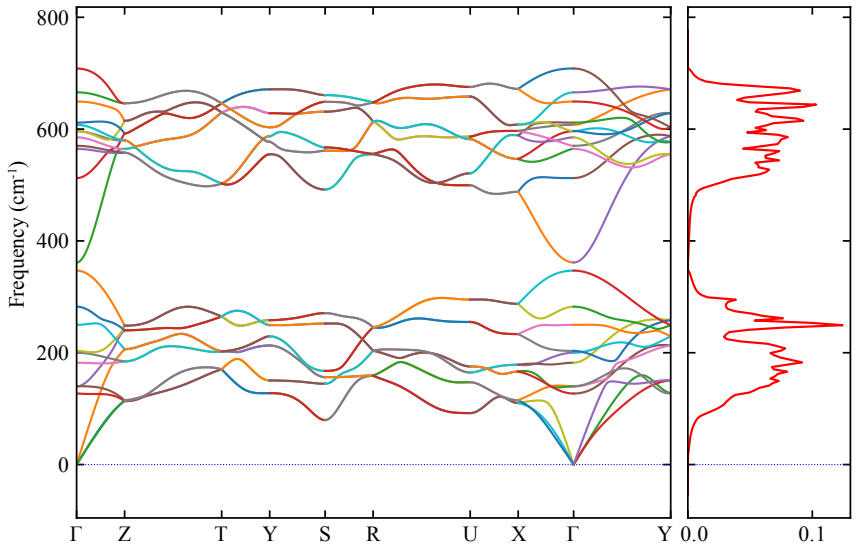

Figure S 12: The PBE+U_{eff}=3.5 eV phonon band structure and density of states for the *Pnma* structure of TcN at 40 GPa.

References

(1) Poineau, F.; Johnstone, E. V.; Weck, P. F.; Forster, P. M.; Kim, E.; Czerwinski, K. R.; Sattelberger, A. P. β-Technetium Trichloride: Formation, Structure, and First-Principles Calculations. *Inorganic Chemistry* **2012**, *51*, 4915–4917.

(2) Silva, G. W. C.; Poineau, F.; Ma, L.; Czerwinski, K. R. Application of electron microscopy in the observation of technetium and technetium dioxide nanostructures. *Inorganic Chemistry* **2008**, *47*, 11738–11744.

(3) Prescher, C.; Prakapenka, V. B. DIOPTAS: a program for reduction of two-dimensional X-ray diffraction data and data exploration. *High Pressure Research* **2015**, *35*, 223–230.

(4) Toby, B. H.; Von Dreele, R. B. GSAS-II: the genesis of a modern open-source all purpose crystallography software package. *Journal of Applied Crystallography* **2013**, *46*, 544–549.

(5) Hohenberg, P.; Kohn, W. Inhomogeneous Electron Gas. *Phys. Rev.* **1964**, *136*, B864–B871.

(6) Kohn, W.; Sham, L. J. Self-Consistent Equations Including Exchange and Correlation Effects. *Phys. Rev.* **1965**, *140*, A1133–A1138.

(7) Perdew, J. P.; Burke, K.; Ernzerhof, M. Generalized Gradient Approximation Made Simple. *Phys. Rev. Lett.* **1996**, *77*, 3865–3868.

(8) Liechtenstein, A. I.; Anisimov, V. I.; Zaanen, J. Density-functional theory and strong interactions: Orbital ordering in Mott-Hubbard insulators. *Phys. Rev. B* **1995**, *52*, R5467–R5470.

(9) Dudarev, S. L.; Botton, G. A.; Savrasov, S. Y.; Humphreys, C. J.; Sutton, A. P. Electron-energy-loss spectra and the structural stability of nickel oxide: An LSDA+U study. *Phys. Rev. B* **1998**, *57*, 1505–1509.

(10) Horton, M. K.; Montoya, J. H.; Liu, M.; Persson, K. A. High-throughput prediction of the ground-state collinear magnetic order of inorganic materials using Density Functional Theory. *npj Computational Materials* **2019**, *5*, 64.

(11) Cococcioni, M.; de Gironcoli, S. Linear response approach to the calculation of the effective interaction parameters in the LDA + U method. *Phys. Rev. B* **2005**, *71*, 035105.

(12) Lawler, K. V.; Childs, B. C.; Mast, D. S.; Czerwinski, K. R.; Sattelberger, A. P.; Poineau, F.; Forster, P. M. Molecular and Electronic Structures of M2O7 (M = Mn, Tc, Re). *Inorganic Chemistry* **2017**, *56*, 2448–2458.

(13) Pack, J. D.; Monkhorst, H. J. "Special points for Brillouin-zone integrations"—a reply. *Phys. Rev. B* **1977**, *16*, 1748–1749.

(14) Methfessel, M.; Paxton, A. T. High-precision sampling for Brillouin-zone integration in metals. *Phys. Rev. B* **1989**, *40*, 3616–3621.

(15) Blöchl, P. E. Projector augmented-wave method. *Phys. Rev. B* **1994**, *50*, 17953–17979.

(16) Ganose, A. M.; Jackson, A. J.; Scanlon, D. O. sumo: Command-line tools for plotting and analysis of periodic *ab initio* calculations. *Journal of Open Source Software* **2018**, *3*, 717.

(17) Bradley, C. J.; Cracknell, A. P. *The Mathematical Theory of Symmetry in Solids*; Clarendon Press: Oxford, 1972.

(18) Wu, X.; Vanderbilt, D.; Hamann, D. R. Systematic treatment of displacements, strains, and electric fields in density-functional perturbation theory. *Phys. Rev. B* **2005**, *72*, 035105.

(19) Togo, A.; Tanaka, I. First principles phonon calculations in materials science. *Scr. Mater.* **2015**, *108*, 1–5.

(20) Siska, E.; Smith, D.; Childs, C.; Koury, D.; Forster, P. M.; Lawler, K. V.; Salamat, A. β-Technetium: An allotrope with a nonstandard volume-pressure relationship. *Phys. Rev. Materials* **2021**, *5*, 063603.

(21) Moruzzi, V. L.; Marcus, P. M. Antiferromagnetism in 4d transition metals. *Phys. Rev. B* **1990**, *42*, 10322–10328.

(22) Oguchi, T.; Freeman, A. Magnetically induced tetragonal lattice distortion in antiferromagnetic fcc Mn. *Journal of Magnetism and Magnetic Materials* **1984**, *46*, L1–L4.

(23) Duschanek, H.; Mohn, P.; Schwarz, K. Antiferromagnetic and ferromagnetic gamma-manganese generalisation of the fixed-spin-moment method. *Physica B: Physics of Condensed Matter* **1990**, *161*, 139–142.

(24) Schieffer, P.; Krembel, C.; Hanf, M.; Bolmont, D.; Gewinner, G. Stabilization of a face-centered-cubic Mn structure with the Ag lattice parameter. *Journal of Magnetism and Magnetic Materials* **1997**, *165*, 180 – 184.

(25) Schirmer, B.; Feldmann, B.; Sokoll, A.; Gauthier, Y.; Wuttig, M. Tetragonal distortion of Mn films on $Cu_3Au(100)$. *Phys. Rev. B* **1999**, *60*, 5895–5903.

(26) Kaiser, A. B. Magnetic moment fluctuations in chromium. *Journal of Magnetism and Magnetic Materials* **1984**, *43*, 213–216.

(27) Fei, Y.; Brosh, E. Experimental study and thermodynamic calculations of phase relations in the Fe–C system at high pressure. *Earth and Planetary Science Letters* **2014**, *408*, 155–162.

(28) Yang, J.; Fei, Y.; Hu, X.; Greenberg, E.; Prakapenka, V. B. Effect of Carbon on the Volume of Solid Iron at High Pressure: Implications for Carbon Substitution in Iron Structures and Carbon Content in the Earth's Inner Core. *Minerals* **2019**, *9*, 720.

(29) Nguyen, K. T.; Hiep Vuong, V.; Nguyen, T. N.; Nguyen, T. T.; Yamamoto, T.; Hoang, N. N. Unusual hydrogen implanted gold with lattice contraction at increased hydrogen content. *Nature Communications* **2021**, *12*, 1560.

(30) Kitagawa, J.; Sakaguchi, K.; Hara, T.; Hirano, F.; Shirakawa, N.; Tsubota, M. Interstitial Atom Engineering in Magnetic Materials. *Metals* **2020**, *10*, 1644.

(31) Oganov, A. R.; Glass, C. W. Crystal structure prediction using ab initio evolutionary techniques: Principles and applications. *The Journal of Chemical Physics* **2006**, *124*, 244704.

(32) Oganov, A. R.; Lyakhov, A. O.; Valle, M. How Evolutionary Crystal Structure Prediction Works–and Why. *Accounts of Chemical Research* **2011**, *44*, 227–237.

(33) Lyakhov, A. O.; Oganov, A. R.; Stokes, H. T.; Zhu, Q. New developments in evolutionary structure prediction algorithm USPEX. *Computer Physics Communications* **2013**, *184*, 1172–1182.

(34) Zhao, Z. L.; Bao, K.; Duan, D. F.; Jin, X. L.; Tian, F. B.; Li, D.; Liu, B. B.; Cui, T. Ideal stoichiometric technetium nitrides under pressure: A first-principles study. *Journal of Superhard Materials* **2014**, *36*, 288–295.

(35) Zhao, Y.-R.; Zhang, G.-T.; Yan, H.-Y.; Bai, T.-T.; Zheng, B.-B.; Yuan, Y.-Q. First-principles investigations of the structure and physical properties for new TcN crystal structure. *Molecular Physics* **2016**, *114*, 1952–1959.

(36) Kim, E.; Weck, P. F.; Mattsson, T. R. Reverse-martensitic hcp-to-fcc transformation in technetium under shock compression. *Journal of Applied Physics* **2018**, *124*, 35903.

(37) Jackson, A. G. *Handbook of Crystallography For Electron Microscopists and Others*; Springer-Verlag New York: New York, 1991; Chapter 6.

(38) Arnold, H. In *International Tables for Crystallography*; Hahn, T., Ed.; International Union of Crystallography, 2006; Vol. A; Chapter 5.1, pp 78–85.